AGU
ADVANCING EARTH AND SPACE SCIENCE

Geophysical Research Letters

Key Points:
- Iceberg calving triggers glacier speedup in the proximity of the ice front when a full-thickness grounded part of the glacier is removed
- Oceanic tides modulate Kangilernata glacier speed daily by 20% at least several km inland
- Maximum strain rates along the calving front are 2–3 times larger than previously thought

Supporting Information:
- Supporting Information S1

Correspondence to:
E. Kane,
kanees@uci.edu

Impact of Calving Dynamics on Kangilernata Sermia, Greenland

Emily Kane[1] , Eric Rignot[1,2] , Jeremie Mouginot[1,3] , Romain Millan[1,3] , Xin Li[1], Bernd Scheuchl[1] , and Mark Fahnestock[4]

[1]Department of Earth System Science, University of California, Irvine, CA, USA, [2]Jet Propulsion Laboratory/Caltech, Pasadena, CA, USA, [3]Universite Grenoble Alpes, CNRS, IRD, Grenoble INP, IGE, Grenoble, France, [4]Geophysical Institute, University of Alaska Fairbanks, Fairbanks, AK, USA

Abstract Iceberg calving is a major component of glacier mass ablation that is not well understood due to a lack of detailed temporal and spatial observations. Here, we measure glacier speed and surface elevation at 3 min intervals using a portable radar interferometer at Kangilernata Sermia, West Greenland, for a period of 2 weeks in July 2016. We detect a 20% diurnal variation in glacier speed in phase with tidal height propagating kilometers inland. We find no speedup from ice shedding off the calving face or the detachment of floating ice blocks but a 30% speedup within a few hundred meters of the ice front that persists for days when calving removes full-thickness grounded ice blocks. Within one ice thickness from the calving front, we detect maximum strain rates 2 to 3 times larger than observable from satellite data, which has implications for studying iceberg calving as a fracturing process.

Plain Language Summary The calving of icebergs from glaciers is a major process of mass loss along the margins of the Greenland Ice Sheet that is poorly understood because it is not well observed with existing systems. We present detailed field observations of glacier speed and elevation acquired every 3 min over 2 weeks along the calving front of a major glacier in Greenland to learn about these processes. We find that the glacier responds to changes in oceanic tide, namely, the glacier speeds up in phase with the tidal height of the ocean waters, and that only calving events that remove full-thickness ice blocks that were resting on the ground, instead of being afloat, affect the glacier speed. Following the calving of grounded ice, the glacier speed is affected for several days but only within a few hundred meters of the ice front. Furthermore, we find that the glacier deformation regime near the ice front is more pronounced than observable from existing spaceborne radars, which has implications for the study of ice fracture, iceberg calving mechanisms, and modeling glacier dynamics.

1. Introduction

The Greenland Ice Sheet has been losing mass for decades at an increasing rate and is contributing significantly to sea level rise (Mouginot et al., 2019). Over the time period 1972–2019, marine terminating glaciers controlled 60% of the ice sheet mass loss (Mouginot et al., 2019; Rignot et al., 2008) versus 40% from surface melt processes. Glacier mass losses result from glacier speedup, increased production of icebergs, ice thinning, and enhanced undercutting of ice by warm ocean waters (Motyka et al., 2003; Rignot et al., 2016). Iceberg calving is a major component of the mass loss at frontal margins (Benn et al., 2007) and the least well understood and modeled component of mass ablation (DeConto & Pollard, 2016). To improve our understanding of iceberg calving and its impact on ice dynamics, it is critical to collect data at the same temporal and spatial scales as that of the physical processes that control these calving events, which means minutes to hours for periods of several days (Cassotto et al., 2018) and with sufficient spatial resolution to observe crack and rift formation. Such combination of high temporal and spatial resolution is not currently available from satellites.

Interferometric synthetic-aperture radar (InSAR) has been used to measure ice velocity at the continental scale on an annual to weekly basis, with a temporal resolution defined by the repeat pass cycle of the satellite (Riesen et al., 2011; Vijay et al., 2019), which is of the order of weeks for most systems, except for the 1 day repeat from the Agenzia Spaziale Italiana's Cosmo SkyMed constellation (Covello et al., 2010; Milillo et al., 2017). Current satellites do not have short-enough repeat cycles to resolve the connection between glacier speedup and processes such as tidal forcing or calving of icebergs on subdaily time scales.
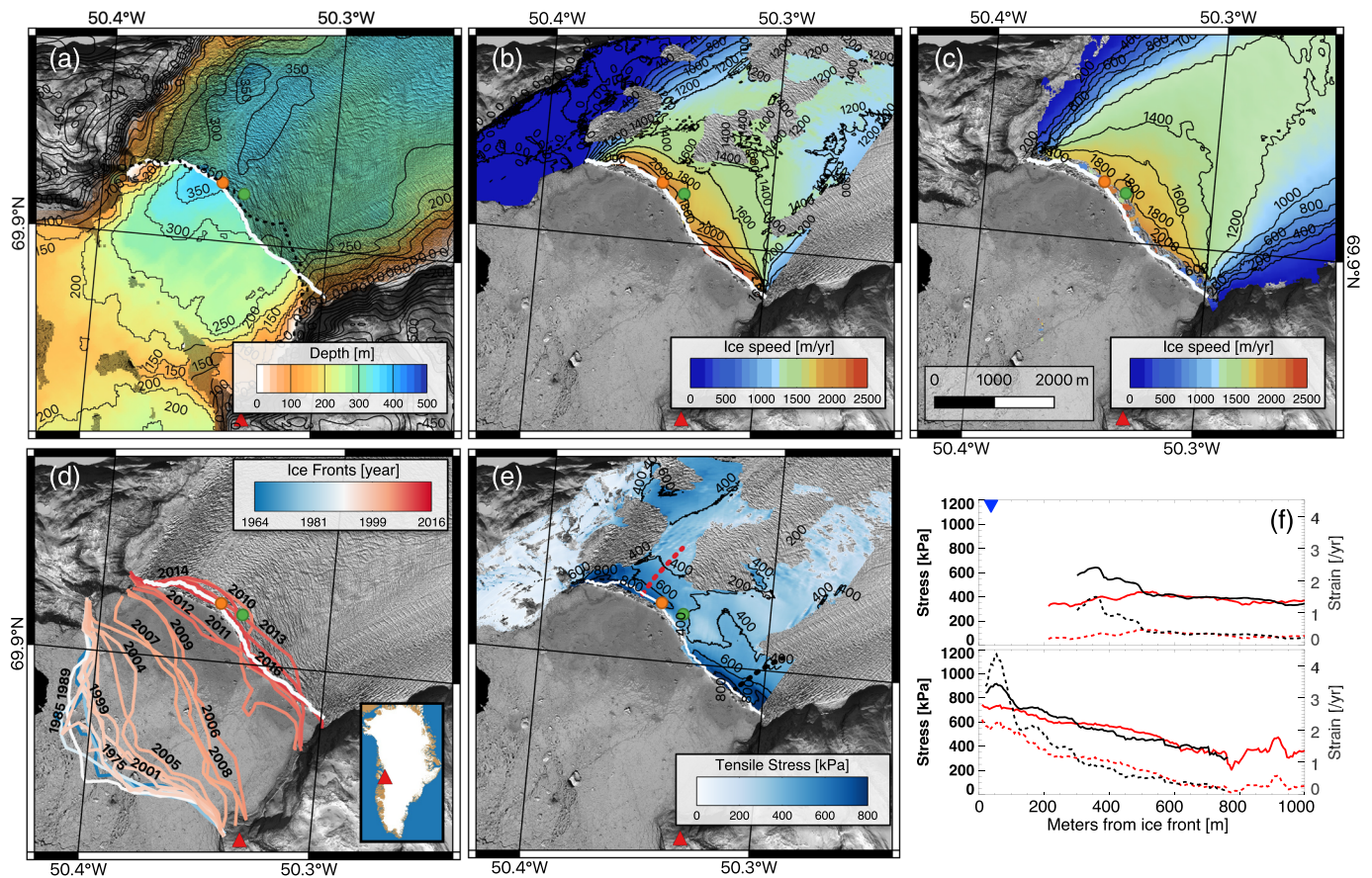
Figure 1. Kangilernata Sermia, Greenland, with (a) OMG bathymetry and BedMachinev3 bed elevation, black dashed line marking the extent of the 2012 MBES coverage beneath the glacier in 2016. (b) GPRI-derived ice speed with contours every 200 m/yr, (c) TerraSAR-X-derived ice speed with contours every 200 m/yr, (d) historical ice front positions from 1964–2016, (e) tensile stress calculated from GPRI with contours every 200 kPa, and (f) tensile stress (solid line) and strain rate (dashed line) along red and black dashed profiles (Figure 1e) from TerraSAR-X (top panel) and GPRI (bottom panel), with ice front after the large calving event (Figure 3a) denoted as blue inverted triangle. Ice front location on 5 July 2016 is white. Green dot is the location for the time series in Figures 2a and 2b. Orange dot is location used in Figure 2c. GPRI is located at red triangle.

Previous remote sensing studies show Greenland glaciers display weekly to seasonal variations in ice speed. Data acquired at Jakonshavn Isbrae with an 11 day repeat cycle using the German Aerospace Center's (DLR) TerraSAR-X showed that ice velocity peaks in the summer months, but daily details within the summer season are few (Joughin et al., 2012). Hourly and daily variations in ice velocity measured using Ground Positioning System (GPS) (Ahlstrøm et al., 2013; Amundson et al., 2008; Nettles et al., 2008; Sugiyama & Gudmundsson, 2004) have shed light on glacier dynamics at subdaily temporal scales, but these in situ methods require a network of observations that is challenging to maintain over a large glacier. The difficulty of maintaining a GPS network near or at a calving front further limits their utility at calving margins.

The Gamma Portable Radar Interferometer (GPRI) has been employed to fill the gap between weekly measurements at the continental scale by satellites and nearly continuous data at discrete locations from GPS. It provides high temporal resolution, typically minutes, at a high spatial resolution, typically a few tens of meters, over many square kilometers of glacier area. Using data collected at subdaily timescales, researchers have been able to link fluctuations in glacier speed with the tidal cycle (Cassotto et al., 2018; Holland et al., 2016; Voytenko et al., 2015; Xie et al., 2018), melt water production (McGrath et al., 2011; Shepherd et al., 2009), melange concentration near the ice front (Cassotto et al., 2015; Xie et al., 2019), and large calving events (Cassotto et al., 2018; Holland et al., 2016). However, much uncertainty remains in our understanding of the relationship between calving events, glacier speed, ice thickness, and bathymetry. In particular, it is not clear why some calving events produce a change in glacier speed while others do not.

Kangilernata Sermia is a 3.5 km wide glacier located in north Disko Bay, Greenland. The glacier was stable on a sill 150 m below sea level from 1964 to 2004, before retreating by 3 km between 2005 and 2010 as the glacier detached from a sill in response to warming ocean waters, and remained relatively stable in waters 350 m deep after 2010 (Figure 1d) (Rignot et al., 2016). Inland of the ice front, the bed elevation remains 200–450 m below sea level for another 30 km (Morlighem et al., 2017). Ice front speed is estimated to have increased from 1.5 m/day (meters per day) in the 1990s to 2.6 m/day between 2005 and 2010 with ice front undercutting by warm ocean waters increasing from 0.7 to 1.9 m/day in the summer months (Rignot et al., 2016).

Here, we use GPRI to document short time scale changes in glacier speed and elevation at a high spatial and temporal resolution for a period of 2 weeks, early in the summer season. We evaluate the effect of tidal variations and iceberg calving on the glacier speed as a function of size, location, and characteristics of the calving events. We compare the results with surface melt production and tidal forcing. We conclude on the importance of calving events on the glacier dynamics and on the insights gained from the short time scale observations of Greenland glaciers.

2. Materials and Methods

2.1. Satellite Data and Bathymetry

We assemble satellite-derived velocity measurements of Kangilernata Sermia from 1984 to present using Landsat-4, 5, 7, and 8, ERS-1 and 2, RADARSAT-1 and 2, ALOS/PALSAR, ENVISAT/ASAR, Sentinel-1a and b, and TerraSAR-X (Mouginot et al., 2017) and updated in Mouginot et al. (2019). The temporal resolution of the data depends on the native repeat cycles of these satellites, which varies from 16 days for Landsat, 35 days for ERS-1/2, 24 days for RADARSAT-1/2, 44 days for ALOS PALSAR, 35 days for Envisat/ASAR, 6 to 12 days for Sentinel-1a/b, and 11 days for TerraSAR-X. We extract velocity values along the 2016 front of Kangilernata Sermia at one location a few hundred meters inland of the ice front (Figure 1).

Fjord bathymetry was mapped with multibeam echo sounding (MBES) in year 2012 to constrain bed elevation to within 1 m (Rignot et al., 2015). Because the glacier re-advanced between 2012 and 2016, the 2012 bathymetry extends about 500 m inland of the 2016 ice front position and thus conveniently provides high quality bed elevation data beneath the ice in 2016 so that we know bed elevation and ice thickness with exceptional and rare precision (Figure 1a).

2.2. GPRI Surface Velocity and Elevation

We deployed a GPRI-II for 2 weeks in July 2016 on the south side of Kangilernata Sermia, at 168 m elevation, 3.5 km from the center of the ice front (Figure 1 and supporting information Figure S1). GPRI is a real-aperture interferometric radar operating at 17.2 GHz, with a range of 16 km, one transmitting antenna and two receiving antennas that scan in azimuth by rotating around a vertical axis, acquiring images range line by range line (Werner et al., 2008). The GPRI operated over a 90° arc scanned during a 20 s data acquisition. Azimuth resolution varies from 28 m at 3.5 km from the ice front to 40 m upstream in the far range of our data. The baseline length is 25 cm. Data are collected at 3 min intervals except when we removed the antennas to protect them from the wind.

We generate a time series of 3 min radar interferograms from GPRI single-look complex images using the Gamma Remote Sensing software package (Werner et al., 2008). We multilook the GPRI data using five range looks and one azimuth look, and smooth the interferograms using an adaptive filter (Goldstein & Werner, 1998) with a filtering window of 64×64 range/azimuth cells with an exponent of nonlinear filtering of 1 to maximize unwrapping without introducing phase jumps. We unwrap the interferometric phase from the filtered interferograms.

The phase difference, ϕ, between successive images determines the line-of-sight (LOS) displacement, $\delta_{los} = \lambda\phi/(4\pi)$, where λ is the wavelength (17.4 mm) (Werner et al., 2008). The displacements are converted into LOS velocities, $V_{los} = \delta_{los}/\delta t$, where δt is the time interval between acquisitions. V_{los} is converted into horizontal speed, V, as $V = V_{los}/[\cos(\alpha)\cos(\zeta)\sin(\theta) - \sin(\alpha)\cos(\theta)]$, where α is the surface slope from the GPRI-derived DEM, ζ is the angle between the TerraSAR-X derived ice flow direction and GPRI look direction, and θ is the radar incidence angle (Kwok & Fahnestock, 1996). We assume no variation in flow direction during the period of observation, which is a reasonable assumption.

Upstream of the ice front, our low grazing illumination angle placed some sections of the ice surface in the shadow of the radar illumination, yielding no signal. Between Days of Year (DOY) 191 and 203 of the campaign, the intensity of the GPRI signal dropped by 3 dB as a result of a weak cable connector. The increase in system noise makes it more difficult to unwrap the phase. We alleviate this issue by unwrapping the phase by blocks. We reconnect blocks by assuming that they are within the same phase ambiguity.

The 3 min displacement results are affected by turbulent atmospheric water vapor which generates phase noise (Riesen et al., 2011; Voytenko, Alon, et al., 2015). To minimize noise, we stack the interferograms in time (Werner et al., 2008) (Figure S2). We performed an analysis to determine optimal stack lengths. We find that atmospheric noise ranges from 250 to 1 m/yr based on stacking windows ranging from 3 min to 6 hr (Figures S2 and S3). We used 30 min stacked data to reduce errors to 15 m/yr on rock and 35 m/yr on ice while preserving the high-resolution quality of the signal (Figure S3).

The dual receiving antennas on the GPRI allow for topographic interferograms between two single-look complex images acquired simultaneously. The interferograms are unwrapped and converted from phase into surface elevation (Strozzi et al., 2012; Voytenko, Dixon, et al., 2015) (Figure S1) and ground controlled using points on land extracted from a WorldView ArcticDEM (Porter et al., 2018). We generate a GPRI DEM using data averaged over 30 min periods. With this amount of data stacking, we estimate the DEM noise level to be less than ± 2.5 m (Figure S3). The 30 min average GPRI-derived Digital Elevation Model (DEM) combined with multibeam coverage under the ice front provides exceptional constraints on ice thickness (± 3 m).

We use the GPRI-derived elevation above mean sea level to calculate ice height above flotation prior to main calving events. We assume that the glacier is grounded when its ice surface elevation is above hydrostatic equilibrium. The height above flotation, $h_f = h - [H((\rho_w - \rho_i)/\rho_w)]$, where ρ_i is the column-averaged density of ice (910 kg/m^3), ρ_w is the density of seawater (1,027 kg/m^3), h is a 30 min average GPRI DEM, and ice thickness, H, is h minus the depth of the sea floor. The density of seawater is the column-averaged density based on conductivity, temperature, and depth (CTD) measurements measured 1 km from the glacier front. The uncertainty in height above flotation combines the uncertainty in h (2.5 m), bathymetry (1 m), and ice and water densities (10%), for an average error value of 4 m which we apply to all ice surface height calculations.

Finally, we calculate the effective tensile strain rate as $\dot{\epsilon}_e{}^2 = 1/2 \left((\max(0, \dot{\epsilon}_1)^2 + (\max(0, \dot{\epsilon}_2)^2) \right)$, where $\dot{\epsilon}_1$ and $\dot{\epsilon}_2$ are the two eigenvectors of the 2-D strain rate tensor derived from the GPRI-derived velocity (Morlighem et al., 2016) (Figure 1c). The strain rate is then converted to tensile stress using a deformation constant of 324 kPa/yr$^{1/3}$ (value for ice at $-5°C$, with an uncertainty of 25%; Cuffey & Paterson, 2010).

2.3. Tracking Calving Events

The multilooked radar backscatter intensity (MLI) data help geolocate the ice front at each acquisition and track the motion of iceberg debris floating at the sea surface with time (Movie S1). The high resolution of these acquisitions makes it possible to provide a timetable of iceberg calving and ice shedding events throughout the survey. For this study, we classify calving events as breakup of ice blocks that produced a detectable retreat of the ice front (>5 m posting) and generated larger-than-average gravity waves in the fjord waters that lasted for tens of minutes. In contrast, we refer to shedding events as breakup of ice blocks that did not produce a detectable change in ice front position and generated gravity waves of less magnitude and shorter duration (minutes). Calving events correspond to full-thickness ice breakup and hence a detectable retreat of the area of grounded ice. Shedding events do not correspond to full ice thickness breakup but to ice slabs or blocks falling off the ice face but not changing its position within the 5 m posting of the data. The MLI imagery also reveals the location of plumes of subglacial discharge as they disturb the ocean surface. Finally, iceberg and ice debris motion retrieved from time series of MLI images provides information about the horizontal circulation of ocean waters in the fjord.

2.4. Tidal Measurements

We installed a HOBO U20 Water Level Logger for 10 days to collect water pressure measurements and allow for tidal height calculations. The tide gauge measured pressure below the water line at a harbor site, about 5 km away from the ice front. Data collection ended before the end of the campaign due to instrument failure.

3. Results

3.1. Velocity Analysis

During the GPRI survey, the 3.5 km wide Kangilernata Sermia moved at an average speed of 1,600 m/yr at the ice front (Figure 1b). Two regions of fast flow are found near the location of meltwater plumes (Movie S1): one along the southern 1.2 km of the ice front with ice speeds in excess of 2,400 m/yr and another located in the deepest section of the fjord (350m depth) with a speed of 2,200 m/yr.

We compare the GPRI-derived velocity data with historical satellite velocity measurements at the center of the glacier, 215 m upstream from the ice front, where both satellite and GPRI data are available (Figure 2a). The speed of 800 m/yr in 1976 did not change until the early 2000s, except in 1994 and 2006 (Mouginot et al., 2019). In 2005, the glacier slowed, then started to speed up as the glacier retreated. The speedup stopped in 2012 when the glacier stabilized to a new bed position (Figure 1d). Peak speed exceeded 2,000 m/yr in 2010–2012, followed by a slowdown to 1,500 m/yr. Ice speed exhibited a seasonal variability of 20–25% during 2004–2018. Seasonal variability is not visible in prior years due to a lack of observations (Figure 2a). Yearly minima of 1,100 m/yr occur in fall and yearly maxima reach 1,900 m/yr in spring.

The GPRI-derived ice speed is within errors of the TerraSAR-X data (Figures 2a, 2b, and S4), which provides confidence in the measurements. In addition, the GPRI data reveal that the glacier experiences diurnal to subdiurnal velocity variations of ± 200 m/yr that extend over almost the entire glacier area imaged by GPRI. Maximum speeds occur around midday at 2,100 m/yr and minimum speeds occur in early morning at 1,570 m/yr (Figure 2c). Superimposed on that diurnal variation, we observe a lower frequency modulation in speed over several days. The modulation in speed is more apparent when compared with tidal forcing. The survey started on DOY 187 during spring tides before transitioning to neap tides on DOY 194 (Figure 2d). We find a correlation of 0.71 between tidal pressure and GPRI-derived ice speed with a 1 hr delay during spring tides (DOY 188–191) and a correlation of 0.63 with the same delay during neap tides (DOY 193–196). During the transition from spring to neap tides, the correlation drops to 0.19. The positive correlation between tidal pressure and speed decreases inland from 0.7 within 300 m of the ice front to 0.3 about 1 km from the ice front.

Following Gudmundsson (2007), we model the glacier speed as a function of tidal pressure, δP, using a Weertman's sliding law (Cuffey & Paterson, 2010). The total speed is $u = (1/r+1)u_b$, where r is a sliding ratio equal to 25, and the sliding speed, $u_b = C\tau_b^m$, where $C = 12\times 10^{-5}$ m/day/kPa^{-m}, the sliding exponent $m = 3$, and τ_b is the basal drag. Basal drag varies around a mean value modulated by tidal pressure, $\tau_b = \bar{\tau}_b + K\delta P$, where the local stress ratio K is chosen to be 0.2. We calculate $\bar{\tau}_b = 35$ kPa based on the mean glacier speed over the entire period and allow a quadratic excursion of ± 9 kPa in $\bar{\tau}_b$ during the survey period to best fit the residuals in mean speed. The value of K is close to that used by Gudmundsson (2007). We varied the sliding ratio r to optimize the model fit and found a sliding ratio of 25. Despite the model simplicity, we obtain a good fit with the data, except perhaps for the brief period between DOY 193 and 195 (Figure S5).

Daily averaged runoff values from the RACMO2.3 model (Noël et al., 2015) for the Kangilernata Sermia basin vary from 0.026 to 0.048 kg/m^2/day over the study period (Figure 2e). We find no correlation between daily runoff and daily averaged ice velocity. At the 95% confidence interval, the squared Pearson correlation coefficient R^2 ranges from 0.045 ($P = 0.18$) at the ice front to 0.064 ($P = 0.22$) about 1 km inland. We conclude that over the short time period of our survey (2 weeks), we could not detect the influence of runoff on glacier speed.

3.2. Calving Event Analysis

The largest calving event occurred on 12 July 2016 (DOY 194) at 15:08 UTC, as the tide was receding. An approximately 650 m long by 105 m wide ice block detached from the ice front in about 9 min. The detached block split into two pieces that moved away from the ice front within minutes (Movie S1). The detachment was accompanied by an immediate increase in speed of the ice front from 1,750 to 2,400 m/yr, or 37% (Figure 3e). The speedup did not propagate more than 0.5 km upstream. The speedup decreased by 7% after the detachment but persisted for the rest of the survey at about 30% above the initial state. We cannot attribute the persistence of the speedup to the calving event, however, since other phenomena may have contributed to maintaining a higher speed, including the tidal forcing or changes in subglacial hydrology. The calved area was 42,500 m^2, of which $79 \pm 6\%$ was afloat and $8,850 \pm 2,800$ m^2 or $21 \pm 6\%$ was grounded. The volume of grounded ice removed was 3.4×10^6 m^3.
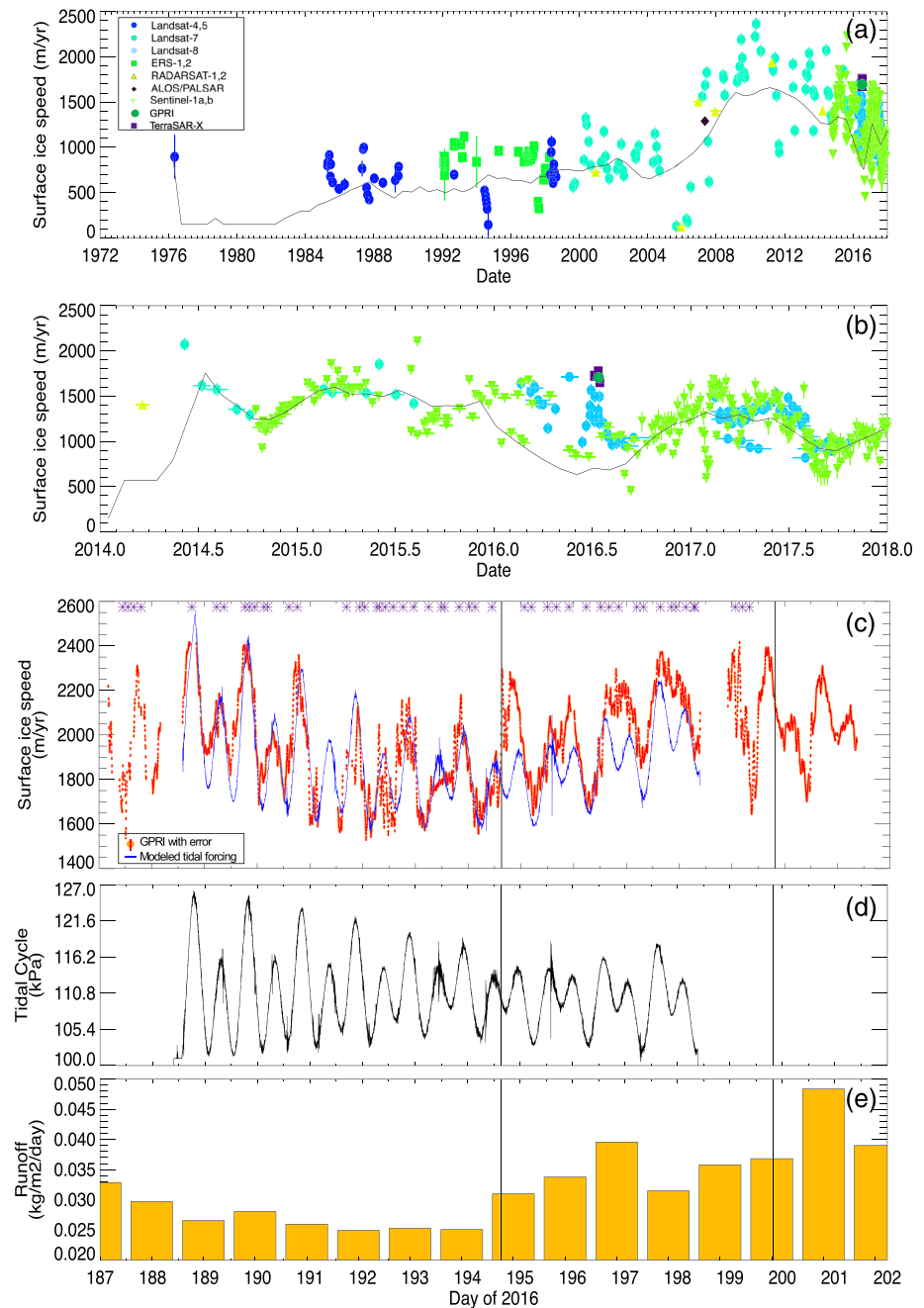
Figure 2. Time series of ice velocity for Kangilernata Sermia, Greenland, derived at location of green dot in Figure 1 from (a) satellite data for 1976–2018 with a 6 month average plotted in black and (b) for 2014–2018 with a monthly average plotted in black. (c) GPRI-derived velocity at location of orange dot in Figure 1 for 5 July 2016 to 19 July 2016 versus tidal forcing from a model. Purple stars denote timing of shedding events. (d) Tidal amplitude in kilopascal (kPa). (e) Daily average runoff from the RACMO2.3 surface mass balance model. Black vertical lines indicate two large calving events examined in Figure 3.

The second largest calving event occurred on 17 July 2016 (DOY 199) at 19:31 UTC. This calving event detached a piece approximately 400 m long by 65 m wide, from roughly the same region (Figure 3b), but with no change in speed (Figure 3f). The calved area was 29,000 m^2, of which $5,300 \pm 2,100$ m^2 or $18 \pm 7\%$ was grounded, corresponding to an ice volume of 1.8×10^6 m^3, hence approximately half in size compared to the largest calving event. During the remainder of the survey, we witnessed many shedding events but none with detectable impact on glacier speed (Figure 2). The changes in speed did not propagate more than
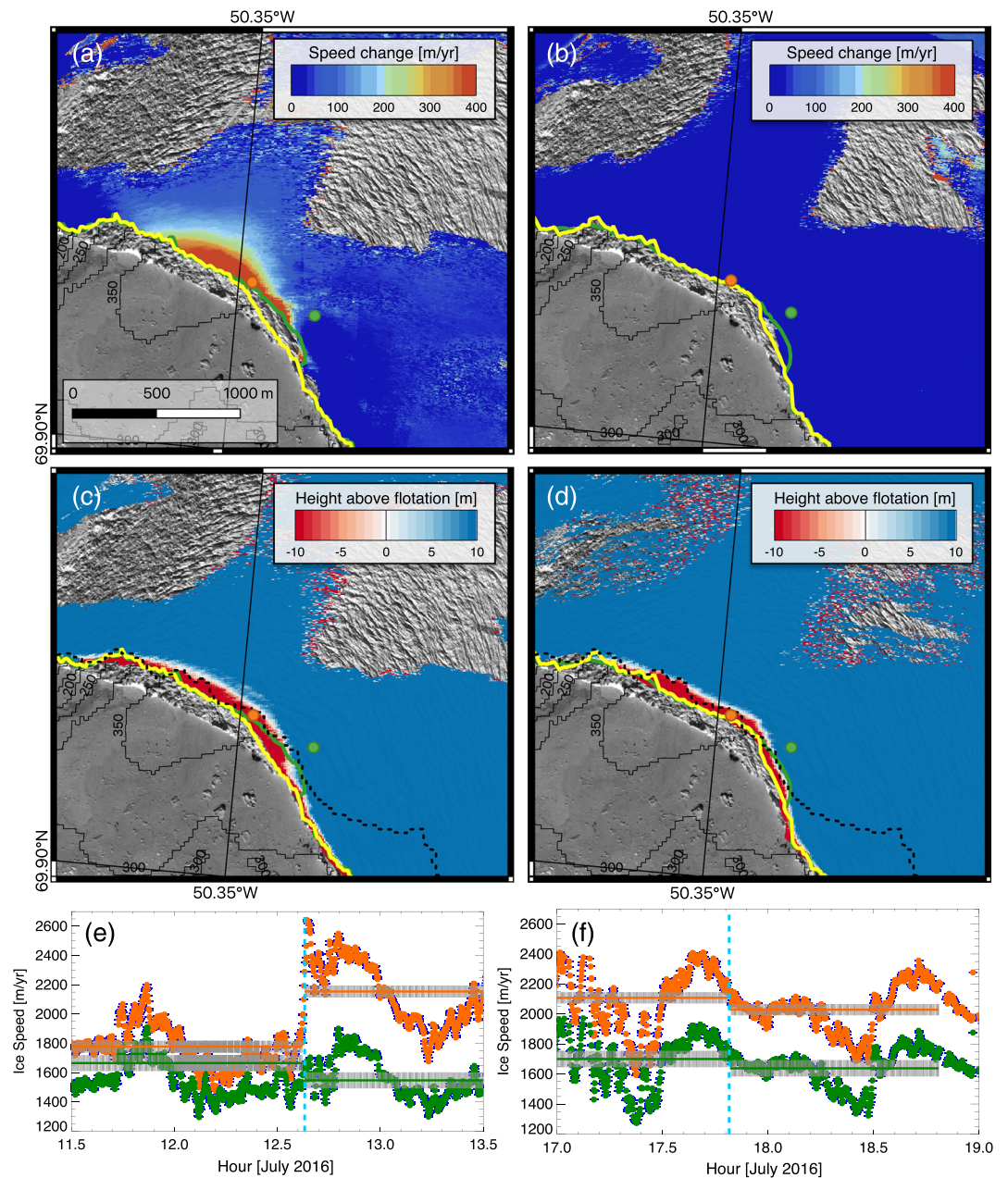
Figure 3. Change in velocity of Kangilernata Sermia for (a) calving event on 12 July 2016 and (b) 17 July 2016, with the height above floatation before the calving event in (c) and (d), respectively. (e, f) Change in speed plotted as the difference in average speed 1 hr before and 1 hr after calving. Bathymetry shown with black solid contours. Ice front positions before and after the calving events are colored yellow and green, respectively. Black dashed line outlines where MBES data exist under the glacier. Panels (e) and (f) are 30 min-averaged GPRI-derived ice speed at the orange and green dots in (a)–(d) around each calving event (cyan dashed line). Orange and green horizontal lines show 24 hr average ice speed before and after calving events with gray bar outlining error. The green and orange dots are the same as in Figures 1 and 2.

about one ice thickness inland, in contrast to the changes associated with ocean tide which effected the entire region imaged by the GPRI, or more than 2 km (Figure S6).

3.3. Strain Rate Analysis

The effective strain rate derived from GPRI is high along a narrow band about 300 m wide, or one ice thickness, along the ice front, with values up to 4/yr versus 0.5 to 1/yr immediately upstream (Figure 1f). Such values of the strain rate are exceptionally high. The strain rates peak within 50 to 80 m from the ice front.

We detect a peak strain rate of 4.5/yr along the eastern flank versus 2.5/yr along the western flank. Such high strain rates are not measurable from the TerraSAR-X-derived velocity because speckle tracking is limited to areas at least a few hundred meters from the ice front due to spatial averaging. We employed speckle tracking with smaller-sized windows, from the nominal 128×96 pixels window (about $212\,\text{m} \times 216\,\text{m}$ in size) that insures no data gap to a 32×24 pixels window (about $54\,\text{m} \times 54\,\text{m}$) which is the minimum-sized window to guarantee a reasonable signal to noise ratio. We could not detect the glacier speed in the narrow region near the front even with the smaller size window (Figure S2). The band of ice speed near the ice front is therefore uniquely revealed in the GPRI data using the interferometric phase at the 5 m spacing.

4. Discussion

Subdaily acquisitions give insights into the complex temporal dynamics of the glacier. From the time series of satellite data, we detect strong interannual, seasonal, and weekly variations but gain no insight about daily variations. Averaged over several days, the TSX and GPRI measurements agree but miss the impact of tides and calving events on glacier dynamics (Figures 2a and 2b).

The influence of tides on glacier velocity has been studied in Greenland and Antarctica with differing results. Rutford Ice Stream varies in phase with the tides at fortnightly timescales with the highest speeds at spring tide and lowest at neap tide (Gudmundsson, 2006). Conversely, Helheim and Jakobshavn Glaciers in Greenland and LeConte Glacier in Alaska have out-of-phase relationships with tidal height (Cassotto et al., 2018; Davis et al., 2014; Holland et al., 2016; O'Neel et al., 2001; Podrasky et al., 2014; Voytenko et al., 2015), which is opposite to what we observe at Kangilernata Sermia. Nonlinear responses to changes in tidal height have been noted for glaciers with floating ice shelves (Brunt et al., 2010; King et al., 2010; Makinson et al., 2012; Padman et al., 2018). We interpret the tidal variations in speed of Kangilernata as caused by tidal modulations of the basal stress by an amount proportional to the tidal pressure, so that basal sliding increases at high tide. In other studies, however, the interpretation was that seawater pressure exerts more backforce on the glacier at high tide. We conclude that the influence of tides on glacier speed is not fully understood. A GPS survey of Helheim glacier reported a daily cycle several km upstream of the glacier terminus attributed to enhanced sliding caused by meltwater production (Holland et al., 2016). We find no relationship between 12 hr stacked GPRI-derived ice velocity and runoff for Kangilernata Sermia.

Calving events observed on tide water glaciers, including with GPRI, do not always affect glacier speed (Cassotto et al., 2018; Podrasky et al., 2014; Voytenko et al., 2015). Our observations suggest that only the detachment of full-thickness grounded ice blocks affects the glacier speed, which is possible to verify in a unique fashion for Kangilernata because of the high quality bathymetry data available at the glacier front. In addition, as for other studies, we find that the change in speed only affects the area near the ice front, not extending far inland, typically about one ice thickness. This finding is consistent with a glacier force balance analysis that dictates that ice blocks already afloat in the ocean have no effect on basal resistance or lateral drag and hence should not affect the glacier speed when removed, whereas grounded ice blocks will reduce basal resistance when they detach from the ice front. We posit that for other glaciers as well, it is likely that only calving events detaching grounded ice blocks affect the glacier speed.

In the ensuing hours and days following the calving event, the glacier speed in the proximity of the calving event did not return to its original state, but the effect only effected the ice within less than 1 km of the ice front. We posit that the time it takes for the glacier to resume its original speed at the ice front is equivalent to the time it takes for a new piece of grounded ice to replace the detached piece of grounded ice, here equivalent to 2 to 3 weeks at the current glacier speed, which is similar to the time scales reported in other studies (Cassotto et al., 2018). As mentioned earlier, a different phase of the tidal forcing or a change in subglacial hydrology could have also contributed to the change in glacier speed after the calving event. The lack of speed upstream of the ice front indicates that the stress coupling between the ice front and the remainder of the glacier decays quickly, within one ice thickness.

The analysis of strain rates reveals the presence of a narrow band of high stresses near the ice front where calving occurs. Morlighem et al. (2016) uses a calving law based on the von Mises (VM) stress. Choi et al. (2018) compared different calving laws and concluded that the VM calving law produced the best fit with observations. In that approach, calving occurs when the tensile stress exceeds a threshold σ_{max}. Here, we use a deformation constant of $324\,\text{kPa/yr}^{1/3}$ (value for ice at $-5°\text{C}$, with an uncertainty of 25%

Cuffey & Paterson, 2010) to convert the strain rates into stresses. With this selection of deformation constant, we calculate stresses ranging from 600 to 900 kPa near the calving margin. Near the largest calving event, the tensile stress was 700 kPa (Figure 1e), which suggests σ_{max} values close to the breaking strength of ice at 1 MPa. In contrast, near the ice front, satellite measurements indicate stress values that remain below 500 kPa, that is, which largely underestimate the peak stresses. A low value of 500 kPa for σ_{max} would overestimate calving rates if employed in a numerical model. We recommend that other glaciers be examined in a similar fashion to evaluate σ_{max}. Caution should be exercised when interpreting strain rate records based on coarse-resolution velocity measurements from speckle tracking or optical tracking that average data over many hundreds of meters.

The application of optical and radar satellites has been transformative for mapping ice velocity in Greenland and Antarctica and documenting long-term and seasonal variations. GPRI studies reveal important information missing from these measurements. In particular, an abrupt glacier speedup coincident with a calving event is difficult to identify if data averaging exceeds 3 hr (Figure S2) and maximum strain rates along calving margins are missing from speckle tracking data with a long repeat cycle. These findings reinforce the need to track ice motion using the interferometric phase at the pixel level instead of speckle tracking over several hundred meters. To do so, satellite data must be acquired at a shorter time scale, typically subdaily. While GPRI is useful to examine processes taking place at that temporal scale, it can only be deployed on a few glaciers over limited periods.

5. Conclusions

We present the first subhourly observations of speed and elevation of Kangilernata Sermia in western Greenland using GPRI to investigate its calving dynamics. We find that the glacier experiences strong diurnal velocity fluctuations of 20% that are positively correlated with tidal pressure and that affect the entire glacier far inland. In contrast, the only calving event that affected glacier speed was one that removed a full-thickness grounded ice block. While the change in speed consecutive to a large calving event extended to a large region around the zone of detachment, the effect did not propagate far inland and hence did not have a major impact on glacier dynamics. In terms of deformation rates, we detect strain rates and stresses 2 to 3 times larger than reported previously along calving fronts using satellite measurements, which has implications for understanding and modeling the break up of ice into icebergs.

Data Availability Statement

Bathymetry data are available publicly at Caltech's Jet Propulsion Laboratory (https://omg.jpl.nasa.gov). Satellite ice velocity data have been deposited in University of California, Irvine Dryad (https://datadryad.org/stash/dataset/, https://doi.org/10.7280/D1MM37, https://doi.org/10.7280/D1GW91, https://doi.org/10.7280/D1595V, and https://doi.org/10.7280/D11H3X) as well as GPRI ice velocity data and average DEM (doi:10.7280/D1R085).

References

Ahlstrøm, A. P., Andersen, S. B., Andersen, M. L., Machguth, H., Nick, F. M., Joughin, I., & Box, J. E. (2013). Seasonal velocities of eight major marine-terminating outlet glaciers of the Greenland Ice Sheet from continuous in situ GPS instrument. *Earth System Science Data*, 5(2), 277–287.

Amundson, J. M., Truffer, M., Lüthi, M. P., Fahnestock, M., West, M., & Motyka, R. J. (2008). Glacier, fjord, and seismic response to recent large calving events, Jakobshavn Isbræ, Greenland. *Geophysical Research Letters*, 35, L22501. https://doi.org/10.1029/2008GL035281

Benn, D. I., Warren, C. R., & Mottram, R. H. (2007). Calving processes and the dynamics of calving glaciers. *Earth-Science Reviews*, 82(3-4), 143–179. https://doi.org/10.1016/j.earscirev.2007.02.002

Brunt, K. M., King, M. A., Fricker, H. A., & MacAyeal, D. R. (2010). Flow of the Ross Ice Shelf, Antarctica, is modulated by the ocean tide. *Journal of Glaciology*, 56(195), 157–161. https://doi.org/10.3189/002214310791190875

Cassotto, R., Fahnestock, M., Amundson, J. M., Truffer, M., Boettcher, M. S., De La Peña, S., & Howat, I. (2018). Non-linear glacier response to calving events, Jakobshavn Isbræ, Greenland. *Journal of Glaciology*, 1–16. https://doi.org/10.1017/jog.2018.90

Cassotto, R., Fahnestock, M., Amundson, J. M., Truffer, M., & Joughin, I. (2015). Seasonal and interannual variations in ice melange and its impact on terminus stability, Jakobshavn Isbræ, Greenland. *Journal of Glaciology*, 61(225), 76–88. https://doi.org/10.3189/2015JoG13J235

Choi, Y., Morlighem, M., Wood, M., & Bondzio, J. H. (2018). Comparison of four calving laws to model Greenland outlet glaciers. *Cryosphere*, 12(12), 3735–3746. https://doi.org/10.5194/tc-12-3735-2018

Covello, F., Battazza, F., Coletta, A., Lopinto, E., Fiorentino, C., Pietranera, L., & Zoffoli, S. (2010). COSMO-SkyMed an existing opportunity for observing the Earth. *Journal of Geodynamics*, 49(3–4), 171–180. https://doi.org/10.1016/j.jog.2010.01.001

Cuffey, K., & Paterson, W. (2010). *The physics of glaciers* (4th ed., p. 693). Burlington, MA: Elsevier.

Davis, J., De Juan, J., Nettles, M., Elosegui, P., & Andersen, M. (2014). Evidence for non-tidal diurnal velocity variations of Helheim Glacier, East Greenland. *Journal of Glaciology*, *60*(224), 1169–1180. https://doi.org/10.3189/2014JoG13J230

DeConto, R. M., & Pollard, D. (2016). Contribution of Antarctica to past and future sea-level rise. *Nature*, *531*(7596), 591–597. https://doi.org/10.1038/nature17145

Goldstein, R. M., & Werner, C. L. (1998). Radar interferogram filtering for geophysical applications. *Geophysical Research Letters*, *25*(21), 4035–4038.

Gudmundsson, G. H. (2006). Fortnightly variations in the flow velocity of Rutford Ice Stream, West Antarctica. *Nature*, *444*(7122), 1063–1064. https://doi.org/10.1038/nature05430

Gudmundsson, G. H. (2007). Tides and the flow of Rutford Ice Stream, West Antarctica. *Journal of Geophysical Research*, *112*, F04007. https://doi.org/10.1029/2006JF000731

Holland, D. M., Voytenko, D., Dixon, T., Mei, J., Parizek, B., Vaňková, I., & Holland, D. (2016). An intensive observation of calving at Helheim Glacier, East Greenland. *Oceanography*, *29*(4), 46–61. https://doi.org/10.5670/oceanog.2016.98

Joughin, I., Smith, B. E., Howat, I. M., Floricioiu, D., Alley, R. B., Truffer, M., & Fahnestock, M. (2012). Seasonal to decadal scale variations in the surface velocity of Jakobshavn Isbrae, Greenland: Observation and model-based analysis: Jakobshavn Isbrae, observation/analysis. *Journal Geophysical Research*, *117*, F02030. https://doi.org/10.1029/2011JF002110

King, M. A., Murray, T., & Smith, A. M. (2010). Non-linear responses of Rutford Ice Stream, Antarctica, to semi-diurnal and diurnal tidal forcing. *Journal of Glaciology*, *56*(195), 167–176. https://doi.org/10.3189/002214310791190848

Kwok, R., & Fahnestock, M. (1996). Ice sheet motion and topography from radar interferometry. *IEEE Transactions on Geoscience and Remote Sensing*, *34*(1), 189–200. https://doi.org/10.1109/36.481903

Makinson, K., King, M. A., Nicholls, K. W., & Hilmar Gudmundsson, G. (2012). Diurnal and semidiurnal tide-induced lateral movement of Ronne Ice Shelf, Antarctica: Tidal movement of Ronne Ice Shelf. *Geophysical Research Letters*, *39*, L10501. https://doi.org/10.1029/2012GL051636

McGrath, D., Colgan, W., Steffen, K., Lauffenburger, P., & Balog, J. (2011). Assessing the summer water budget of a moulin basin in the Sermeq Avannarleq ablation region, Greenland Ice Sheet. *Journal of Glaciology*, *57*(205), 954–964. https://doi.org/10.3189/002214311798043735

Milillo, P., Rignot, E., Mouginot, J., Scheuchl, B., Morlighem, M., Li, X., & Salzer, J. T. (2017). On the short-term grounding zone dynamics of Pine Island Glacier, West Antarctica observed with COSMO-SkyMed interferometric data: PIG grounding line dynamics. *Geophysical Research Letters*, *44*(20), 10,436–10,444. https://doi.org/10.1002/2017GL074320

Morlighem, M., Bondzio, J., Seroussi, H., Rignot, E., Larour, E., Humbert, A., & Rebuffi, S. (2016). Modeling of Store Gletscher's calving dynamics, West Greenland, in response to ocean thermal forcing. *Geophysical Research Letters*, *43*, 2659–2666. https://doi.org/10.1002/2016GL067695

Morlighem, M., Williams, C. N., Rignot, E., An, L., Arndt, J. E., Bamber, J. L., & Zinglersen, K. B. (2017). Bedmachine V3: Complete bed topography and ocean bathymetry mapping of Greenland from multibeam echo sounding combined with mass conservation. *Geophysical Research Letters*, *44*, 11,051–11,061. https://doi.org/10.1002/2017GL074954

Motyka, R. J., Hunter, L., Echelmeyer, K. A., & Connor, C. (2003). Submarine melting at the terminus of a temperate tidewater glacier, LeConte Glacier, Alaska, U.S.A. *Annals of Glaciology*, *36*, 57–65.

Mouginot, J., Rignot, E., Bjørk, A. A., van den Broeke, M., Millan, R., Morlighem, M., & Wood, M. (2019). Forty-six years of Greenland Ice Sheet mass balance from 1972 to 2018. *Proceedings of the National Academy of Sciences*, *116*, 9239–9244. https://doi.org/10.1073/pnas.1904242116

Mouginot, J., Rignot, E., Scheuchl, B., & Millan, R. (2017). Comprehensive annual ice sheet velocity mapping using Landsat-8, Sentinel-1, and RADARSAT-2 data. *Remote Sensing*, *9*(4), 364. https://doi.org/10.3390/rs9040364

Nettles, M., Larsen, T. B., Elósegui, P., Hamilton, G. S., Stearns, L. A., Ahlstrøm, A. P., & Forsberg, R. (2008). Step-wise changes in glacier flow speed coincide with calving and glacial earthquakes at Helheim Glacier, Greenland. *Geophysical Research Letters*, *35*, L24503. https://doi.org/10.1029/2008GL036127

Noël, B., Van De Berg, W., Van Meijgaard, E., Kuipers Munneke, P., Van De Wal, R., & Van Den Broeke, M. (2015). Evaluation of the updated regional climate model RACMO2. 3: Summer snowfall impact on the Greenland Ice Sheet. *The Cryosphere*, *9*(5), 1831–1844.

O'Neel, S., Echelmeyer, K. A., & Motyka, R. J. (2001). Short-term flow dynamics of a retreating tidewater glacier: LeConte Glacier, Alaska, U.S.A. *Journal of Glaciology*, *47*(159), 567–578. https://doi.org/10.3189/172756501781831855

Padman, L., Siegfried, M. R., & Fricker, H. A. (2018). Ocean tide influences on the Antarctic and Greenland Ice Sheets: Tide influences on ice sheets. *Reviews of Geophysics*, *56*, 142–184. https://doi.org/10.1002/2016RG000546

Podrasky, D., Truffer, M., Lüthi, M., & Fahnestock, M. (2014). Quantifying velocity response to ocean tides and calving near the terminus of Jakobshavn Isbræ, Greenland. *Journal of Glaciology*, *60*(222), 609–621. https://doi.org/10.3189/2014JoG13J130

Porter, C., Morin, P., Howat, I., Noh, M. J., Bates, B., Peterman, K., & Bojesen, M. (2018). ArcticDEM. Harvard Dataverse V1. https://doi.org/10.7910/DVN/OHHUKH

Riesen, P., Strozzi, T., Bauder, A., Wiesmann, A., & Funk, M. (2011). Short-term surface ice motion variations measured with a ground-based portable real aperture radar interferometer. *Journal of Glaciology*, *57*(201), 53–60.

Rignot, E., Box, J. E., Burgess, E., & Hanna, E. (2008). Mass balance of the Greenland Ice Sheet from 1958 to 2007. *Geophysical Research Letters*, *35*, L20502. https://doi.org/10.1029/2008GL035417

Rignot, E., Fenty, I., Xu, Y., Cai, C., & Kemp, C. (2015). Undercutting of marine-terminating glaciers in West Greenland: Glacier undercutting by ocean waters. *Geophysical Research Letters*, *42*(14), 5909–5917. https://doi.org/10.1002/2015GL064236

Rignot, E., Xu, Y., Menemenlis, D., Mouginot, J., Scheuchl, B., Li, X., & Fleurian, B. D. (2016). Modeling of ocean-induced ice melt rates of five West Greenland glaciers over the past two decades. *Geophysical Research Letters*, *43*, 6374–6382. https://doi.org/10.1002/2016GL068784

Shepherd, A., Hubbard, A., Nienow, P., King, M., McMillan, M., & Joughin, I. (2009). Greenland Ice Sheet motion coupled with daily melting in late summer. *Geophysical Research Letters*, *36*, L01501. https://doi.org/10.1029/2008GL035758

Strozzi, T., Werner, C., Wiesmann, A., & Wegmuller, U. (2012). Topography mapping with a portable real-aperture radar interferometer. *Geophysical Research Letters*, *9*, 277–281. https://doi.org/10.1109/LGRS.2011.2166751

Sugiyama, S., & Gudmundsson, G. H. (2004). Short-term variations in glacier flow controlled by subglacial water pressure at Lauteraargletscher, Bernese Alps, Switzerland. *Journal of Glaciology*, *50*(170), 353–362.

Vijay, S., Khan, S. A., Kusk, A., Solgaard, A. M., Moon, T., & Bjørk, A. A. (2019). Resolving seasonal ice velocity of 45 Greenlandic glaciers with very high temporal details. *Geophysical Research Letters*, *46*(3), 1485–1495. https://doi.org/10.1029/2018GL081503

Voytenko, D., Alon, S., Holland, D., Dixon, T., Christianson, K., & Walker, R. (2015). Tidally driven ice speed variation at Helheim Glacier, Greenland, observed with terrestrial radar interferometry. *Journal of Glaciology*, *61*(226), 301–308. https://doi.org/10.3189/2015JoG14J173

Voytenko, D., Dixon, T. H., Howat, I. M., Gourmelen, N., Lembke, C., Werner, C. L., & Oddsono, B. (2015). Multi-year observations of Breiamerkurjökull, a marine-terminating glacier in southeastern Iceland, using terrestrial radar interferometry. *Journal of Glaciology*, *61*(225), 42–54. https://doi.org/10.3189/2015JoG14J099

Werner, C., Strozzi, T., Wiesmann, A., & Wegmuller, U. (2008). A real-aperture radar for ground-based differential interferometry. In *Proc. Int. Geosci. Rem. Sens. Symp. (IGARSS)*, *3*, Boston, MA, USA, pp. III210–III213.

Xie, S., Dixon, T. H., Holland, D. M., & Voytenko, D. (2019). Vaňková, I Rapid iceberg calving following removal of tightly packed pro-glacial mélange. *Nature Communications*, *10*(1), 3250. https://doi.org/10.1038/s41467-019-10908-4

Xie, S., Dixon, T. H., Voytenko, D., Deng, F., & Holland, D. M. (2018). Grounding line migration through the calving season at Jakobshavn Isbræ, Greenland, observed with terrestrial radar interferometry. *Cryosphere*, *12*(4), 1387–1400. https://doi.org/10.5194/tc-12-1387-2018